

Multi-Agent Variational Occlusion Inference Using People as Sensors

Masha Itkina¹, Ye-Ji Mun², Katherine Driggs-Campbell², and Mykel J. Kochenderfer¹

Stanford University¹, University of Illinois Urbana-Champaign²

{mitkina, mykel}@stanford.edu {yejimun2, krdc}@illinois.edu

Abstract: Autonomous vehicles must reason about spatial occlusions in urban environments to ensure safety without being overly cautious. Prior work explored occlusion inference from observed social behaviors of road agents. Inferring occupancy from agent behaviors is an inherently multimodal problem; a driver may behave in the same manner for different occupancy patterns ahead of them (e.g., a driver may move at constant speed in traffic or on an open road). Past work, however, does not account for this multimodality, thus neglecting to model this source of aleatoric uncertainty in the relationship between driver behaviors and their environment. We propose an occlusion inference method that characterizes observed behaviors of human agents as sensor measurements, and fuses them with those from a standard sensor suite. To capture the aleatoric uncertainty, we train a conditional variational autoencoder with a discrete latent space to learn a multimodal mapping from observed driver trajectories to an occupancy grid representation of the view ahead of the driver. Our method handles multi-agent scenarios, combining measurements from multiple observed drivers using evidential theory to solve the sensor fusion problem. Our approach is validated on a real-world dataset, outperforming baselines and demonstrating real-time capable performance. Our code is available at <https://github.com/sisl/MultiAgentVariationalOcclusionInference>.

Keywords: occlusion inference, variational autoencoders, autonomous driving

1 Introduction

Safe autonomous navigation in the presence of occlusions in a cluttered, human environment is an open problem for mobile robot perception and decision making [1]. It is common in robotics to assume occluded regions to be either free [2] or occupied space [3], which may result in either dangerous or overly cautious behavior. While humans suffer from similar limitations, they are able to make inferences about these unobserved spaces using insights from prior experience as well as semantic and geometric information. While driving, humans intuitively anticipate potential hazards, even when they are occluded, by observing the behavior of other road agents. For instance, if another vehicle brakes sharply, a driver may infer the presence of an occluded obstacle (e.g., a pedestrian) ahead, necessitating them to act cautiously. Likewise, autonomous vehicles should be capable of making inferences about occluded regions in order to safely interact with human road users.

Occlusion inference in the context of interaction has been explored from the perspectives of mapping [4], inverse reinforcement learning (IRL) [5], and pedestrian tracking [6]. Afolabi et al. [4] used driver models as additional sensor information to provide “measurements” within regions of occlusion in an environment map, coining the term *People as Sensors (PaS)*. They showed that occupancy grid maps (OGMs) [7] are a useful environment representation for fusing insights from observed interactive behaviors with traditional sensor outputs. The OGM representation does not require prior knowledge of the environment structure and can handle partially observed and previously unseen road users, making it more generalizable compared to object-centric alternatives [8].

Occlusion inference based on observed behaviors is an intrinsically multimodal problem. For example, a driver may drive at the speed limit in traffic (occupied space ahead) or on an empty road (free space ahead). Similarly, a driver may brake for a single pedestrian or a group of pedestrians, which would yield different occupancy patterns. The occlusion inference model must handle this irreducible (i.e., aleatoric) uncertainty to accurately represent the space of possible inferred maps. However, prior work [4, 5, 6] often does not account for the multimodality in the occluded region’s

occupancy given a driver behavior, thus neglecting this source of aleatoric uncertainty.

Inspired by PaS [4], we use observed road agent behaviors as additional sensor information into an OGM of the environment. We extend PaS to incorporate distributional multimodality and to a multi-agent framework where several human drivers can provide measurements within the occluded regions of the map. To do this, we present an occlusion inference algorithm with two stages. First, we learn a *driver sensor model* that maps an observed driver trajectory to a discrete set of possibilities for the OGM of the space ahead of the driver. To account for the multimodality in the inferred occupancy, we use a conditional variational autoencoder (CVAE) [9] with a discrete latent space for the driver sensor model. In the second stage, we fuse the spatial predictions inferred from multiple observed driver trajectories into the environment map using a multi-agent sensor fusion mechanism based in evidential theory [10].

The goal of our approach is to enhance current perception and inference techniques specifically targeting unmeasured, occluded spaces by combining ideas from mapping, human modeling, and sensor fusion. We present a framework that can handle complex multi-agent settings and validate the proposed technique using real-world data. Our contributions are as follows:

- We learn a sensor model for human drivers end-to-end using a CVAE architecture with a discrete latent space that captures distributional multimodality.
- Our occlusion inference method allows us to consider multiple human drivers (modeled as sensors) through evidential sensor fusion.
- We demonstrate real-time capable performance of our method and outperform baselines on a cluttered, unsignalized intersection in the INTERACTION dataset [11].

2 Related Works

Temporary Occlusions Numerous methods have been proposed for tracking objects through temporary occlusions (i.e., when an object comes in and out of view). In robot manipulation, a self-occlusion results when the robot temporarily occludes objects of interest from its view. This temporary issue is typically dealt with using specialized architectures and features [12, 13, 14]. These works usually assume a static background, which is not the case in urban driving settings where the environment is continually evolving. Dequaire et al. [15] handle temporary occlusions in an urban environment by having the neural network learn to hallucinate previously observed objects in occluded regions from memory. Our method differs from memory-based occlusion inference by considering interactive behavior on the road as an additional information source to infer fully occluded, previously unobserved obstacles in a self-supervised manner.

Inpainting Urban Scenes A separate line of work from computer vision uses inpainting of the environment to fill in the occluded portions of the scene. Inpainting has been used to infer bird’s-eye view (BeV) semantics of the partially occluded static environment behind foreground obstacles [16, 17] as well as the partially occluded foreground obstacles themselves [18]. Inpainting of the BeV environment semantics provides a more comprehensive estimate of the navigable space and can improve path planning performance as compared to the original more restricted, occluded view [19]. In occupancy mapping, Gaussian processes have been used to interpolate occupancy behind partially occluded obstacles [20, 21, 22]. Most of these methods assume static environments, and none of them reason about fully occluded, dynamic obstacles.

Occlusion Inference using Environment Structure Other works infer fully occluded road agents using prior knowledge of road agent dynamics and the environment structure. Typically, these ap-

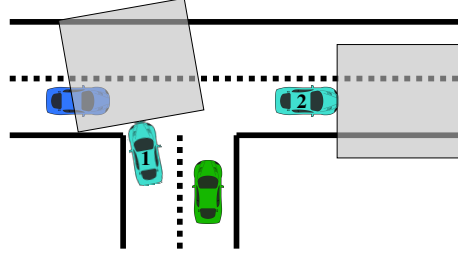


Figure 1: Our proposed occlusion inference approach. The learned driver sensor model maps behaviors of visible drivers (cyan) to an OGM of the environment ahead of them (gray). The inferred OGMs are then fused into the ego vehicle’s (green) map. Our goal is to infer the presence or absence of occluded agents (blue). Driver 1 is waiting to turn left, occluding oncoming traffic from the ego vehicle’s view. Driver 1 being stopped should indicate to the ego that there may be oncoming traffic; and thus it is not safe to proceed with its right turn. Driver 2 is driving at a constant speed. This observed behavior is not enough to discern whether the vehicle is traveling in traffic or on an open road. We aim to encode such intuition into our occlusion inference algorithm.

proaches use this information to define reachable regions for potentially occluded obstacles [23, 24]. Hypothesized road agents can be assumed to always exist at the limits of the observable space [25] or in occluded locations on the road that might lead to collisions with the ego vehicle [24]. Their velocity profiles can be predetermined by their class [23] or using information from a digital map [26]. These approaches often consider worst-case occlusion scenarios that may lead to overly conservative behavior and do not exploit observable interactions to inform the occlusion inference.

Social Occlusion Inference Methods that use observed social interactions to infer fully occluded obstacles are most closely related to our work. Hara et al. [6] infer the existence of an approaching car from outside of the field of view of a camera using observed pedestrian reactions. Sun et al. [5] perform behavior-based occlusion inference using IRL to learn a cost function that acts as the driver sensor model. These costs update the belief over visible object states and hidden states (e.g., pre-defined driving styles). Their approach is validated in simulation. Afolabi et al. [4] uncover driver actions by clustering over trajectories and then learn occupancy probabilities for the OGM for each action. This two-step process forms their driver sensor model. The formulation is demonstrated on a crosswalk scenario with a single sensor vehicle and a single occluded pedestrian in simulation. We propose an end-to-end approach, which learns a multimodal mapping from driver trajectories to the OGM ahead of the driver, accounting for aleatoric uncertainty. We generalize the technique to multi-agent settings using ideas from sensor fusion and validate our method on real-world data.

3 Problem Formulation

We consider the problem of occlusion inference in a cluttered, urban setting from the perspectives of mapping, human modeling, and sensor fusion. We represent the local environment surrounding the ego vehicle as an OGM $\mathcal{M}_{ego}^{obs} \in [0, 1]^{H \times W}$, where H and W are its dimensions. The OGM is generated using ray tracing from a range-bearing sensor in the standard sensor suite (e.g., LiDAR or radar). The occlusion inference task then becomes imputing occupancy probabilities in regions of occlusion within this OGM. Occluded regions will refer to the subset of cells in the OGM that receive no sensor measurements at a time step. Assuming highly accurate sensors, the observed occupied grid cells have an occupancy probability of 1, while free cells have a probability of 0. Occluded grid cells are denoted with 0.5 occupancy probability. Without loss of generality, we further assume that the OGMs do not incorporate temporal history. The omniscient OGM $\mathcal{M}_{ego}^{gt} \in \{0, 1\}^{H \times W}$ contains the ground truth occupancy from a BeV without occlusions. We aim to infer the occupancy of the occluded grid cells (where $\mathcal{M}_{ego}^{obs} = 0.5$) from observed human driver behaviors.

We assume that our ego vehicle is equipped with a perception system that is able to detect, track, and estimate the pose of visible road agents, which is a reasonable assumption given existing computer vision capabilities [11, 27]. We denote the state of an observed human driver h at time t as,

$$s_h^t = [x_h^t, y_h^t, \psi_h^t, v_{x,h}^t, v_{y,h}^t, a_{x,h}^t, a_{y,h}^t], \quad (1)$$

capturing the position, orientation, velocity, and acceleration. Each human driver h observes the environment ahead of them represented as another OGM $\mathcal{M}_h \in \{0, 1\}^{H_h \times W_h}$, where H_h and W_h denote the dimensions of the human driver’s OGM. As visualized in Fig. 1, the view represented by \mathcal{M}_h may be occluded from the ego vehicle. We hypothesize that the region ahead of the human driver may be partially recovered from their observed behavior. Thus, we use the observed behaviors and interactions of human drivers to impute occupancy in occluded regions of \mathcal{M}_{ego}^{obs} .

4 Multi-Agent Variational Occlusion Inference

Our proposed occlusion inference approach, which we illustrate in Fig. 1, consists of two steps. First, we learn a driver sensor model that maps an observed behavior of a human driver h , represented as a trajectory $s_h^{1:T}$ over a time horizon T , to the OGM representation \mathcal{M}_h of the environment ahead of them at time step T . Second, the inferred OGMs \mathcal{M}_h for all observed drivers h are fused into \mathcal{M}_{ego}^{obs} in regions of occlusion as additional sensor measurements. The driver sensor model and multi-sensor fusion are described in detail in the following sections.

Driver Sensor Model We draw on the vast literature in human behavior modeling [28] to build our driver sensor model. A common approach in interaction modeling is to discretize the set of human behaviors [29, 30]. CVAEs have been shown to successfully discretize this set of behavior and capture the aleatoric uncertainty over these behaviors [31, 32]. As such, we formulate our driver

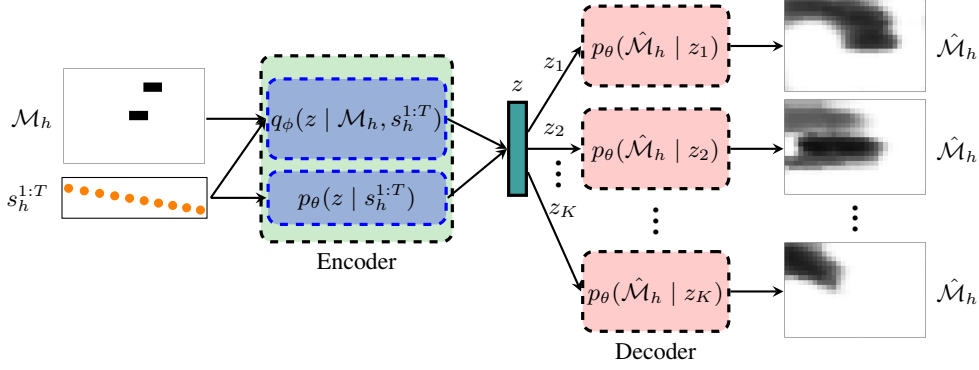


Figure 2: The proposed driver sensor model. The CVAE consists of two encoders and a decoder. The encoders learn the categorical prior and posterior distributions $p_\theta(z | s_h^{1:T})$ and $q_\phi(z | s_h^{1:T}, \mathcal{M}_h)$, respectively, over the discrete latent variable $z \in \{1, \dots, K\}$, where $s_h^{1:T}$ is the observed trajectory of driver h , \mathcal{M}_h is the ground truth OGM of the view ahead of driver h , and θ and ϕ are network parameters. The decoder takes as input each latent class z_k and outputs the estimated environment view ahead of the driver $\hat{\mathcal{M}}_h$. During inference, the network produces a multimodal categorical prior over the possible OGMs $\hat{\mathcal{M}}_h$ given an input trajectory $s_h^{1:T}$.

sensor model as a CVAE that maps observed trajectories to a discrete latent space that captures the multimodal possibilities for the environment ahead of the driver.

The CVAE, which we illustrate in Fig. 2, consists of two encoders and a decoder, as inspired by the setup of Itkina et al. [33]. The encoders represent the categorical prior and posterior distributions $p_\theta(z | s_h^{1:T})$ and $q_\phi(z | s_h^{1:T}, \mathcal{M}_h)$, respectively, over the discrete latent variable $z \in \{1, \dots, K\}$, where θ and ϕ are network parameters. The latent encoding z is distributed according to the posterior during training and the prior during inference. It is then passed through the decoder to output an estimated environment view for the driver $\hat{\mathcal{M}}_h \in [0, 1]^{H_h \times W_h}$.

The learned categorical prior $p_\theta(z | s_h^{1:T})$ accounts for the multimodal distribution over the inferred environment. During inference, the network takes the trajectory $s_h^{1:T}$ as input and outputs the categorical prior corresponding to the possible OGMs $\hat{\mathcal{M}}_h$ for each latent class z_k for $k \in \{1, \dots, K\}$.

We train the CVAE with a modified evidence lower bound (ELBO) loss,

$$\begin{aligned} \mathcal{L}(\mathcal{M}_h, s_h^{1:T}; \theta, \phi) = & -\mathbb{E}_{z \sim q_\phi(z | s_h^{1:T})} [\log p_\theta(\mathcal{M}_h | z)] \\ & + \beta \text{KL}(q_\phi(z | s_h^{1:T}, \mathcal{M}_h) || p_\theta(z | s_h^{1:T})) - \alpha I_{q_\phi}(\mathcal{M}_h; z), \end{aligned} \quad (2)$$

where α and β are hyperparameter weights, KL is the Kullback–Leibler divergence, and $I_{q_\phi}(\mathcal{M}_h; z)$ is the approximate mutual information between \mathcal{M}_h and z under the posterior distribution $q_\phi(z | s_h^{1:T}, \mathcal{M}_h)$ [32]. We use the prior $p_\theta(z | s_h^{1:T})$ as a proxy for the posterior distribution and acquire $p_\theta(z)$ by summing over the batch following [32]. By keeping the number of latent classes K small, we are able to compute the reconstruction loss term (first term in Eq. (2)) exactly without resorting to sampling approximation techniques such as the Gumbel-Softmax reparameterization [34, 35]. To address the class imbalance between occupied and free cells in the data, the reconstruction loss is weighted according to one minus the fraction of occupied or free cells in a batch. The full loss is computed as the average of Eq. (2) over all the training examples in a batch.

Multi-Sensor Fusion for Occlusion Inference The driver sensor model outputs K estimated OGMs $\hat{\mathcal{M}}_h$ and the associated learned categorical prior $p_\theta(z | s_h^{1:T})$ given an observed trajectory $s_h^{1:T}$ for driver h . These OGMs for all visible drivers h need to be incorporated into \mathcal{M}_{ego}^{obs} . The occlusion inference problem then becomes a sensor fusion task. We use evidential theory [10], a popular sensor fusion technique [36], to fuse the measurements from the driver sensor model into \mathcal{M}_{ego}^{obs} . Evidential theory is able to discern conflicting information (e.g., two differing sensor measurements) from lack of information (e.g., a region of occlusion). It does so by considering the power set of exhaustive hypotheses. In the case of OGMs, our hypothesis set is $\Omega = \{O, F\}$, where O is the occupied class and F is the free class. The power set of the hypotheses is then $2^\Omega = \{\emptyset, \{O\}, \{F\}, \{O, F\}\}$. Evidential theory defines a belief mass function $m : 2^\Omega \rightarrow [0, 1]$ such that $\sum_{A \subseteq \Omega} m(A) = 1$. Since a grid cell cannot be neither free nor occupied, the belief mass

for the empty set is zero: $m(\emptyset) = 0$. A non-zero belief mass on set $\{O, F\}$ represents a lack of evidence that discerns between the occupied and free hypotheses. Belief mass functions from different sensors can be combined using Dempster-Shafer’s rule [10].

We begin the sensor fusion process by heuristically transforming the probabilities in $\hat{\mathcal{M}}_h$ into a belief mass for each observed human driver h in the vicinity of the ego vehicle, as follows:

$$m_{h,c}(\{O\}) = \delta \hat{\mathcal{M}}_{h,c}, \quad m_{h,c}(\{F\}) = \delta(1 - \hat{\mathcal{M}}_{h,c}), \quad (3)$$

where c is a grid cell and $\delta \in [0, 1]$ is a hyperparameter. Intuitively, the occupancy probability in $\hat{\mathcal{M}}_{h,c}$ is considered evidence towards the occupied class and, symmetrically, the free probability $1 - \hat{\mathcal{M}}_{h,c}$ is considered evidence towards the free class. Both are scaled down by a factor δ , which represents the uncertainty belief mass $m_{h,c}(\{O, F\}) = 1 - \delta$. We set δ to 0.95 in our experiments.

We incorporate the inferred occupancy estimates only in the occluded cells of \mathcal{M}_{ego}^{obs} since the driver sensor model will be less precise than traditional sensors (e.g., LiDAR) in unoccluded portions of the map. Prior to receiving any measurements in an occluded cell c , we have complete uncertainty in its occupancy, i.e., $m_{ego,c}(\{O, F\}) = 1$. We sequentially update this mass with the measurement masses $m_{h,c}$ of the observed drivers for a single time step using Dempster-Shafer’s rule [10]:

$$m_{ego,c}(A) = m_{ego,c} \oplus m_{h,c}(A) := \frac{\sum_{X \cap Y = A} m_{ego,c}(X) m_{h,c}(Y)}{1 - \sum_{X \cap Y = \emptyset} m_{ego,c}(X) m_{h,c}(Y)}, \quad \forall A, X, Y \in 2^\Omega. \quad (4)$$

The masses $m_{ego,c}$ can then be converted to traditional probabilities using pignistic probability [37]:

$$\hat{\mathcal{M}}_{ego,c}(B) = \sum_{A \in 2^\Omega} m_{ego,c}(A) \frac{|B \cap A|}{|A|}. \quad (5)$$

where B is a singleton hypothesis and $|A|$ is the cardinality of set A (a possible hypothesis).

We compute the likelihood of a fused grid $\hat{\mathcal{M}}_{ego}$ using the learned priors $p_\theta(z \mid s_h^{1:T})$ from the driver sensor model. We assume the trajectory $s_h^{1:T}$ and the latent encoding z data pairs are i.i.d.. Then, the likelihood of $\hat{\mathcal{M}}_{ego}$ is $p(\hat{\mathcal{M}}_{ego}) = \prod_h p_\theta(z \mid s_h^{1:T})$ for all visible drivers h .

5 Experiments

The following section describes the experimental setting used to validate the occlusion inference approach presented in Section 4. We set the number of latent classes to $K = 100$ based on computational time and tractability for the considered baselines. Further experimental and implementation details as well as our CVAE architecture and training scheme are included in Appendix A.

Data Processing To train and test our model, we use data from the GL unsignalized intersection in the INTERACTION dataset [11], which contains highly interactive real-world traffic trajectories from a BeV. We subsample vehicles that serve as the ego vehicle from the available tracks. We then build OGMs around these vehicles, focusing on mapping the region in front of the drivers. We construct the ground truth OGM \mathcal{M}_{ego}^{gt} from the BeV data and the occluded OGM \mathcal{M}_{ego}^{obs} using ray tracing. The ego OGMs are of dimension 70×60 with a grid cell resolution of 1 m. Partially observed vehicles are mapped as fully observed, and only completely occluded vehicles are marked as occluded in \mathcal{M}_{ego}^{obs} . Examples of \mathcal{M}_{ego}^{obs} and \mathcal{M}_{ego}^{gt} are shown in Appendix A. For all drivers visible to an ego vehicle, their position, orientation, velocity, and acceleration are extracted to form the trajectory vector $s_h^{1:T}$ over 1 s of past data sampled at 10 Hz. We filter out all vehicles not observed for a contiguous 1 s from the dataset. An OGM \mathcal{M}_h is constructed for the environment ahead of each visible driver h of dimension 20×30 with a 1 m resolution. Since we consider a relatively small area in front of the driver sensor, we assume \mathcal{M}_h to not have any occlusions.

Baselines We baseline our proposed method against the original PaS approach, referred to as *k-means PaS* [4]. This algorithm first clusters trajectory data over a time interval using k-means. Then given a cluster, the occupancy probability of each cell in $\hat{\mathcal{M}}_h$ for an observed driver h is computed. Since the original work did not consider multiple observed drivers, we incorporate this driver sensor model into our sensor fusion pipeline to perform multi-agent occlusion inference.

K-means PaS does not model the multimodality of the inferred environment given a trajectory. Thus, we additionally consider an extension that uses a Gaussian mixture model (GMM) learned with

Table 1: Our driver sensor model consistently outperforms baselines across metrics on the test set. Bold denotes the best performing model across a metric. Note that IS values are divided by 100. The maximum standard error per grid cell for accuracy and MSE is 0.0007, and per OGM for IS is 0.0022.

Method	Occupied	Free	Overall	Occupied	Free	Overall
	Acc. \uparrow			Top 3 Acc. \uparrow		
K-means PaS [4]	0.512	0.463	0.465	N/A	N/A	N/A
GMM PaS	0.494	0.439	0.440	0.611	0.562	0.557
Ours	0.619	0.601	0.601	0.819	0.773	0.764
	MSE \downarrow			Top 3 MSE \downarrow		
K-means PaS [4]	0.188	0.206	0.206	N/A	N/A	N/A
GMM PaS	0.192	0.211	0.211	0.157	0.166	0.169
Ours	0.293	0.192	0.194	0.145	0.113	0.124
	IS \downarrow			Top 3 IS \downarrow		
K-means PaS [4]	0.205	0.020	0.225	N/A	N/A	N/A
GMM PaS	0.209	0.026	0.235	0.185	0.015	0.209
Ours	0.187	0.017	0.204	0.115	0.007	0.130

the expectation-maximization (EM) [38] algorithm to cluster the trajectories, termed *GMM PaS*. The comparison of our proposed approach to GMM PaS highlights the performance improvements gained from the more expressive CVAE model and learning the OGM end-to-end directly from the trajectory input, rather than first computing the clusters, and then separately inferring the OGM.

Although we focus on comparing different driver sensor models both on their own and within our multi-sensor fusion algorithm, we further ablate our method in Appendix B using a naive averaging strategy in place of the proposed evidential sensor fusion approach. For completeness, we also provide results for the vanilla OGM \mathcal{M}_{ego}^{obs} which has 0.5 probability in occluded cells in Appendix B.

Metrics We consider three core metrics in our evaluation: accuracy, mean squared error (MSE), and image similarity (IS) [39]. To compute accuracy, we threshold the occupancy probability above 0.6 to be occupied, below 0.4 to be free, and those in between to be unknown (0.5). The accuracy and MSE metrics both focus on precision. Since we cannot expect precise recovery of the environment in front of a driver solely from their observed trajectory, we also consider the IS metric. The IS metric was found to be representative of the occlusion inference task in an OGM setting [4]. IS captures the relative structure of the OGMs using the Manhattan distance rather than a one-to-one comparison of individual grid cells. Further details are in Appendix A. Since the data contains an occupancy class imbalance, we break down each metric per occupied and free class, and overall.

To evaluate the ability of GMM PaS and our proposed approach to accurately represent the multimodality of the data, we also consider a multimodal variant of each metric. We take the best metric across the three most likely modes of the GMM and CVAE for the driver sensor model evaluation. We do the same for the full occlusion inference pipeline according to the likelihoods $p(\hat{\mathcal{M}}_{ego})$ described in Section 4. We refer to these metrics as “Top 3”.

6 Results

Driver Sensor Model We compare our proposed CVAE driver sensor model to k-means and GMM PaS baselines in Table 1. Across almost all metrics, the CVAE outperforms the baselines. Despite the difficulty of the task in terms of precision, our model was able to achieve relatively high top 3 accuracy. It outperformed the GMM PaS baseline across all top 3 metrics, reflecting better modeling of the distributional multimodality. The only metric on which the CVAE underperforms the baselines is MSE for the occupied class. We hypothesize this is in part due to the CVAE better capturing multimodality in its latent distribution, resulting in the most likely mode not necessarily being the most accurate mode (multiple modes may have similar likelihoods when multimodality is present). Moreover, the latent spaces learned by the baselines appear to favor occupied cells as compared to that learned by the CVAE. The decoded latent spaces for each model are shown in Appendix B.

Fig. 3 shows exemplary qualitative results for the output of the CVAE model. Two scenarios are depicted: an input deceleration maneuver (Fig. 3a) and a constant speed trajectory (Fig. 3b). Our intuition dictates that the driver in Fig. 3a is likely slowing down due to another road agent ahead or near them. For the driver in Fig. 3b, however, we do not have enough information to conclude if the space ahead of them is occupied since the driver may be traveling at a constant speed in traffic

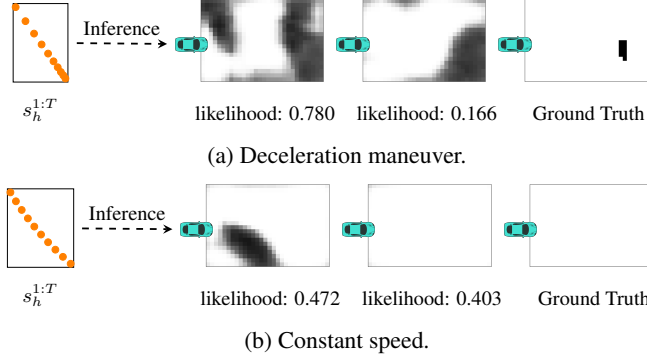


Figure 3: Qualitative results for our proposed CVAE driver sensor model for a deceleration maneuver and a constant speed trajectory. For input trajectories over 1 s ($s_h^{1:T}$), two most likely inferred OGMs $\hat{\mathcal{M}}_h$ are shown, alongside the ground truth OGM \mathcal{M}_h . The OGMs depict free (white), unknown (gray), and occupied (black) space ahead of the driver. The model results align with our intuition: an observed deceleration likely indicates occupied space ahead, whereas a constant speed profile may indicate either free space or traffic ahead.

or on an open road. The CVAE model reflects this intuition. It infers occupied space ahead in its two most likely latent modes for the deceleration case, matching the ground truth. For the constant speed case, it correctly captures the multimodality of the scenario inferring either free or occupied space ahead with similar likelihood in the top two latent modes. These qualitative examples show that the CVAE is able to infer the environment ahead of a driver given their trajectory and correctly capture the multimodality of the associated data distribution.

Multi-Agent Occlusion Inference We now consider the full occlusion inference pipeline. Our proposed approach with the CVAE driver sensor model and evidential sensor fusion runs on average at 0.018 s per time step, which is real-time capable given that typical perception systems operate at 10 Hz [40]. We again baseline our proposed CVAE driver sensor model against k-means and GMM PaS in Table 2. However, now we incorporate the inferences from multiple drivers with the evidential sensor fusion mechanism into \mathcal{M}_{ego}^{obs} to form $\hat{\mathcal{M}}_{ego}$. For the full occlusion inference pipeline, we compute the metrics across only the occluded cells in \mathcal{M}_{ego}^{obs} and ignore the cells in $\hat{\mathcal{M}}_{ego}$ that are thresholded to 0.5. Our approach outperformed the baselines on all metrics except accuracy and MSE for the occupied class. Since we only incorporate the occlusion inference outputs in regions of occlusion for the ego vehicle, this biases the subset of the grid cells that are inferred (e.g., to the side of the vehicle as for driver 75 in Fig. 4a). It appears that for these regions, the baselines lean heavier to the occupied class than the CVAE. Nevertheless, according to the IS metric, the structure of the occupancy in the occluded region continues to be predicted most accurately by the CVAE model.

Fig. 4 illustrates a scenario with two different observed behaviors by a driver sensor. The ego vehicle (green) is waiting for a gap in traffic in order to turn right at the unsignalized intersection. An observed driver 33 is blocking the view of oncoming traffic from the ego while waiting to turn left. In Fig. 4a, driver 33 is stopped due to occluded driver 92 passing by. Our occlusion inference algorithm is able to correctly identify occupied space in the region near driver 92. In Fig. 4b, driver 33 starts moving to make the left turn as there is a gap in traffic. Our method successfully infers free space ahead of this driver, indicating to the ego vehicle that it may be safe to proceed with its right turn. In both cases, our approach is able to provide additional insight about the scene to the ego vehicle as compared to the vanilla OGM \mathcal{M}_{ego}^{obs} with no occlusion inference.

This scene contains several observed drivers and their associated environment inferences. However, not all of these trajectories provide sufficient information to precisely infer the occupancy ahead of the driver (e.g., constant speed driving). Being able to capture the multimodality of the different options for these trajectories thus becomes important. We further illustrate this idea in Appendix B.

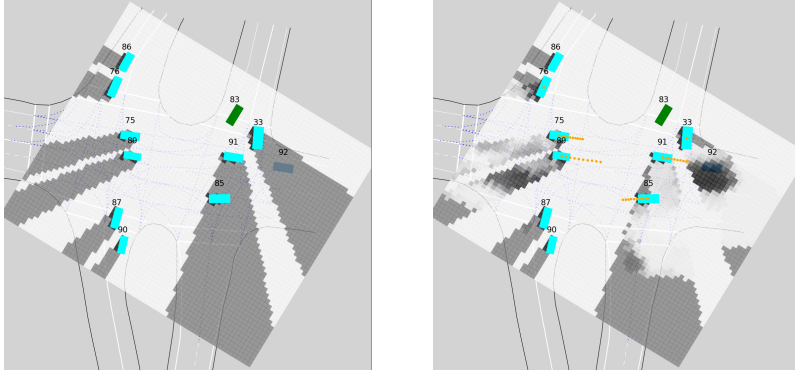
7 Conclusion

We proposed a real-time capable, multi-agent framework for occlusion inference that uses observed human behaviors to inform occluded regions of an ego vehicle’s map. Our approach aims to capture human-like intuition for reasoning about occlusions under uncertainty. Our experiments show that accurately modeling the multimodality of the data distribution improves performance in this setting.

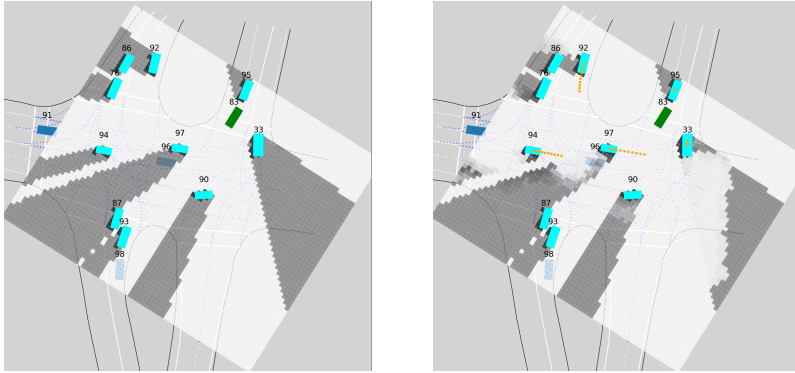
There are several interesting avenues for future work. To filter out uninformative measurements, it would be worthwhile to focus the driver sensor model on only the highly interactive trajectories using ideas from anomaly detection [41]. Furthermore, incorporating HD map information into the driver sensor model could improve the generalizability of the algorithm to different road layouts and allow for better semantic reasoning (e.g., based on navigable space or traffic light state) to inform occlusion inference.

Table 2: Our method outperforms baselines across most considered metrics for the full occlusion inference pipeline in the ego vehicle’s regions of occlusion. Bold denotes the best performance. IS values are divided by 100. The maximum standard error per grid cell for accuracy and MSE is 0.0008, and per OGM for IS is 0.0046.

Method	Occupied	Free	Overall	Occupied	Free	Overall
	Acc. \uparrow			Top 3 Acc. \uparrow		
K-means PaS (Evidential)	0.834	0.680	0.682	N/A	N/A	N/A
GMM PaS (Evidential)	0.838	0.660	0.663	0.860	0.691	0.691
Ours (Evidential)	0.660	0.722	0.722	0.746	0.778	0.774
	MSE \downarrow			Top 3 MSE \downarrow		
K-means PaS (Evidential)	0.146	0.198	0.197	N/A	N/A	N/A
GMM PaS (Evidential)	0.144	0.205	0.204	0.123	0.181	0.181
Ours (Evidential)	0.303	0.171	0.173	0.233	0.136	0.140
	IS \downarrow			Top 3 IS \downarrow		
K-means PaS (Evidential)	1.373	0.027	1.400	N/A	N/A	N/A
GMM PaS (Evidential)	1.393	0.029	1.423	1.277	0.018	1.297
Ours (Evidential)	1.336	0.017	1.353	1.220	0.011	1.232



(a) Stopped vehicle.



(b) Acceleration maneuver.

Figure 4: Qualitative results for the full pipeline using our proposed CVAE driver sensor model. The scenario depicts the ego vehicle (green) waiting to make a right turn. The observed drivers are shown in cyan and their trajectories for the past 1 s ($s_h^{1:T}$) in orange. The vanilla OGM \mathcal{M}_{ego}^{obs} (left) and the fused OGM $\hat{\mathcal{M}}_{ego}$ (right) depict free (white), occluded (gray), and occupied (black) space around the ego. The occupancy patterns inferred by the algorithm match our intuition based on the observed behaviors.

Acknowledgments

We thank Ransalu Senanayake for the enlightening discussions. We thank Spencer M. Richards for his invaluable feedback. This project was made possible with funding from the Ford-Stanford Alliance and a gift from Mercedes-Benz Research & Development North America.

References

- [1] M. Bouton, K. Julian, A. Nakhaei, K. Fujimura, and M. J. Kochenderfer. Utility decomposition with deep corrections for scalable planning under uncertainty. In *International Conference on Autonomous Agents and Multiagent Systems (AAMAS)*, 2018.
- [2] S. Koenig and M. Likhachev. D* lite. In *Conference on Artificial Intelligence (AAAI)*, 2002.
- [3] P. Florence, J. Carter, and R. Tedrake. Integrated perception and control at high speed: Evaluating collision avoidance maneuvers without maps. In *Workshop on the Algorithmic Foundations of Robotics (WAFR)*, 2016.
- [4] O. Afolabi, K. Driggs-Campbell, R. Dong, M. Kochenderfer, and S. Sastry. People as sensors: Imputing maps from human actions. In *International Conference on Intelligent Robots and Systems (IROS)*. IEEE, 2018.
- [5] L. Sun, W. Zhan, C.-Y. Chan, and M. Tomizuka. Behavior planning of autonomous cars with social perception. In *Intelligent Vehicles Symposium (IV)*, pages 207–213. IEEE, 2019.
- [6] K. Hara, H. Kataoka, M. Inaba, K. Narioka, R. Hotta, and Y. Satoh. Predicting vehicles appearing from blind spots based on pedestrian behaviors. In *International Conference on Intelligent Transportation Systems (ITSC)*, pages 1–8. IEEE, 2020.
- [7] A. Elfes. Using occupancy grids for mobile robot perception and navigation. *IEEE Computer*, 22(6):46–57, 1989.
- [8] M. Itkina, K. Driggs-Campbell, and M. J. Kochenderfer. Dynamic environment prediction in urban scenes using recurrent representation learning. In *International Conference on Intelligent Transportation Systems (ITSC)*, pages 2052–2059. IEEE, 2019.
- [9] K. Sohn, H. Lee, and X. Yan. Learning structured output representation using deep conditional generative models. *Advances in Neural Information Processing Systems (NeurIPS)*, 28:3483–3491, 2015.
- [10] A. P. Dempster. A generalization of Bayesian inference. *Classic Works of the Dempster-Shafer Theory of Belief Functions*, pages 73–104, 2008.
- [11] W. Zhan, L. Sun, D. Wang, H. Shi, A. Clause, M. Naumann, J. Kümmerle, H. Königshof, C. Stiller, A. de La Fortelle, and M. Tomizuka. INTERACTION dataset: An international, adversarial and cooperative motion dataset in interactive driving scenarios with semantic maps. *arXiv*, 2019.
- [12] F. Ebert, C. Finn, A. X. Lee, and S. Levine. Self-supervised visual planning with temporal skip connections. In *Conference on Robot Learning (CoRL)*, pages 344–356, 2017.
- [13] Y. Wang, G. N. Narasimhan, X. Lin, B. Okorn, and D. Held. Roll: Visual self-supervised reinforcement learning with object reasoning. In *Conference on Robot Learning (CoRL)*, 2020.
- [14] J. Park and D. Manocha. HMPO: Human Motion Prediction in Occluded Environments for Safe Motion Planning. In *Robotics: Science and Systems*, 2020.
- [15] J. Dequaire, P. Ondruška, D. Rao, D. Wang, and I. Posner. Deep tracking in the wild: End-to-end tracking using recurrent neural networks. *International Journal of Robotics Research*, 37(4-5):492–512, 2018.
- [16] S. Schuster, M. Zhai, N. Jacobs, and M. Chandraker. Learning to look around objects for top-view representations of outdoor scenes. In *European Conference on Computer Vision (ECCV)*, pages 787–802, 2018.

- [17] C. Lu and G. Dubbelman. Semantic foreground inpainting from weak supervision. *Robotics and Automation Letters*, 5(2):1334–1341, 2020.
- [18] P. Purkait, C. Zach, and I. Reid. Seeing behind things: Extending semantic segmentation to occluded regions. In *International Conference on Intelligent Robots and Systems (IROS)*, pages 1998–2005. IEEE, 2019.
- [19] Y. Han, J. Banfi, and M. Campbell. Planning paths through unknown space by imagining what lies therein. In *Conference on Robot Learning (CoRL)*, 2020.
- [20] S. T. O’Callaghan and F. T. Ramos. Gaussian process occupancy maps. *International Journal of Robotics Research*, 31(1):42–62, 2012.
- [21] R. Senanayake and F. Ramos. Bayesian Hilbert maps for dynamic continuous occupancy mapping. In *Conference on Robot Learning (CoRL)*, pages 458–471, 2017.
- [22] R. Senanayake, A. Tompkins, and F. Ramos. Automorphing kernels for nonstationarity in mapping unstructured environments. In *Conference on Robot Learning (CoRL)*, pages 443–455, 2018.
- [23] Y. Nager, A. Censi, and E. Frazzoli. What lies in the shadows? Safe and computation-aware motion planning for autonomous vehicles using intent-aware dynamic shadow regions. In *International Conference on Robotics and Automation (ICRA)*, pages 5800–5806. IEEE, 2019.
- [24] C. Hubmann, N. Quetschlich, J. Schulz, J. Bernhard, D. Althoff, and C. Stiller. A POMDP maneuver planner for occlusions in urban scenarios. In *Intelligent Vehicles Symposium (IV)*, pages 2172–2179. IEEE, 2019.
- [25] H. Chae and K. Yi. Virtual target-based overtaking decision, motion planning, and control of autonomous vehicles. *IEEE Access*, 8:51363–51376, 2020.
- [26] S. Hoermann, F. Kunz, D. Nuss, S. Renter, and K. Dietmayer. Entering crossroads with blind corners. A safe strategy for autonomous vehicles. In *Intelligent Vehicles Symposium (IV)*, pages 727–732. IEEE, 2017.
- [27] H. Caesar, V. Bankiti, A. H. Lang, S. Vora, V. E. Liong, Q. Xu, A. Krishnan, Y. Pan, G. Baldan, and O. Beijbom. nuScenes: A multimodal dataset for autonomous driving. In *Computer Society Conference on Computer Vision and Pattern Recognition (CVPR)*, pages 11621–11631. IEEE/CVF, 2020.
- [28] K. Brown, K. Driggs-Campbell, and M. J. Kochenderfer. A taxonomy and review of algorithms for modeling and predicting human driver behavior. *ArXiv*, 2020.
- [29] I. Kotseruba, A. Rasouli, and J. K. Tsotsos. Joint attention in autonomous driving (JAAD). *arXiv*, 2016.
- [30] T. Bandyopadhyay, C. Z. Jie, D. Hsu, M. H. Ang Jr, D. Rus, and E. Frazzoli. Intention-aware pedestrian avoidance. In *Experimental Robotics*, pages 963–977. Springer, 2013.
- [31] E. Schmerling, K. Leung, W. Vollprecht, and M. Pavone. Multimodal probabilistic model-based planning for human-robot interaction. In *International Conference on Robotics and Automation (ICRA)*, pages 3399–3406. IEEE, 2018.
- [32] T. Salzmann, B. Ivanovic, P. Chakravarty, and M. Pavone. Trajectron++: Dynamically-feasible trajectory forecasting with heterogeneous data. In *European Conference on Computer Vision (ECCV)*, 2020.
- [33] M. Itkina, B. Ivanovic, R. Senanayake, M. J. Kochenderfer, and M. Pavone. Evidential sparsification of multimodal latent spaces in conditional variational autoencoders. *Advances in Neural Information Processing Systems (NeurIPS)*, 33, 2020.
- [34] E. Jang, S. Gu, and B. Poole. Categorical reparameterization with Gumbel-Softmax. In *International Conference on Learning Representations (ICLR)*, 2017.

- [35] C. J. Maddison, A. Mnih, and Y. W. Teh. The Concrete distribution: A continuous relaxation of discrete random variables. In *International Conference on Learning Representations (ICLR)*, 2017.
- [36] L. A. Klein. *Sensor and data fusion: a tool for information assessment and decision making*, volume 138. SPIE Press, 2004.
- [37] P. Smets. Data fusion in the transferable belief model. In *International Conference on Information Fusion (FUSION)*, volume 1, pages PS21–PS33. IEEE, 2000.
- [38] T. K. Moon. The expectation-maximization algorithm. *IEEE Signal Processing Magazine*, 13(6):47–60, 1996.
- [39] A. Birk and S. Carpin. Merging occupancy grid maps from multiple robots. *Proceedings of the IEEE*, 94(7):1384–1397, 2006.
- [40] V. Guizilini, R. Senanayake, and F. Ramos. Dynamic Hilbert maps: Real-time occupancy predictions in changing environments. In *International Conference on Robotics and Automation (ICRA)*, pages 4091–4097. IEEE, 2019.
- [41] V. Chandola, A. Banerjee, and V. Kumar. Anomaly detection: A survey. *ACM Computing Surveys (CSUR)*, 41(3):1–58, 2009.
- [42] S. Hochreiter and J. Schmidhuber. Long short-term memory. *Neural Computation*, 9(8):1735–1780, 1997.
- [43] A. van den Oord, O. Vinyals, and K. Kavukcuoglu. Neural discrete representation learning. In *Advances in Neural Information Processing Systems (NeurIPS)*, pages 6306–6315, 2017.
- [44] S. Bowman, L. Vilnis, O. Vinyals, A. Dai, R. Jozefowicz, and S. Bengio. Generating sentences from a continuous space. In *SIGNLL Conference on Computational Natural Language Learning (CoNLL)*, pages 10–21, 2016.
- [45] D. Kingma and J. Ba. Adam: A method for stochastic optimization. In *International Conference on Learning Representations (ICLR)*, 2015.
- [46] J. L. Bentley. Multidimensional binary search trees used for associative searching. *Communications of the ACM*, 18(9):509–517, 1975.

A Experimental Details

All experiments were performed on an Intel Core i7-6700HQ processor and an NVIDIA 8GB GeForce RTX 1070 GPU.

A.1 Data Split

To process the data, ego vehicle IDs were sampled from the GL intersection in the INTERACTION dataset [11]. For each of the 60 available scenes, a maximum of 100 ego vehicles were chosen. The train, validation, and test set were randomly split based on the ego vehicle IDs accounting for 85%, 5% and 10% of the total number of ego vehicles, respectively. Due to computational constraints, the training set for the driver sensor model was further reduced to have 70,001 contiguous driver sensor trajectories or 2,602,332 time steps of data. The validation set used to select the driver sensor model and the sensor fusion scheme contained 4,858 contiguous driver sensor trajectories or 180,244 time steps and 289 ego vehicles. The results presented in this paper were reported on the test set, which consists of 9,884 contiguous driver sensor trajectories or 365,201 time steps and 578 ego vehicles.

A.2 Example OGMs

We show exemplary ego OGMs in Fig. 5. These OGMs are from the same time step as Fig. 4a. Examples of predicted driver sensor and ground truth OGMs can be seen in Fig. 3. We intentionally chose the dimensions of the driver sensor OGMs (20×30) to be smaller than the dimensions of the ego OGMs (70×60) to reflect that the driver sensors are likely reacting to the local environment closest to them.

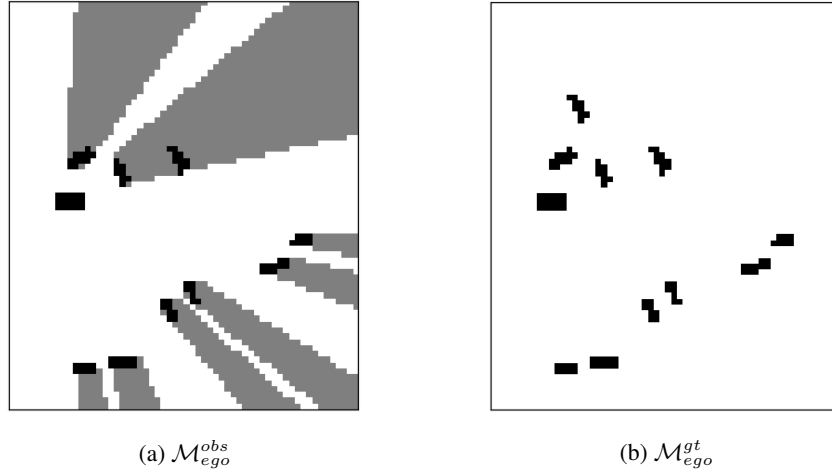


Figure 5: Example ego vehicle OGMs. They depict free (white), occluded (gray), and occupied (black) space around the ego vehicle, which is located in the middle left of each OGM. \mathcal{M}_{ego}^{obs} contains occluded regions, whereas \mathcal{M}_{ego}^{gt} is omniscient.

A.3 CVAE Driver Sensor Model Architecture and Training

We set the number of latent classes in the CVAE to $K = 100$ based on computational time and tractability for the considered baselines. We standardize the trajectory data $s_h^{1:T}$ to have zero mean and unit standard deviation. The prior encoder in the model consists of an LSTM [42] with a hidden dimension of 5 to process the 1 s of trajectory input data $s_h^{1:T}$. A linear layer then converts the output into a K -dimensional vector that goes into a softmax function, producing the prior distribution. The posterior encoder extracts features from the ground truth input \mathcal{M}_h using a VQ-VAE backbone [43] with a hidden dimension of 4. These features are flattened and concatenated with the LSTM output from the trajectory data, and then passed into a linear layer and a softmax function, producing the posterior distribution. The decoder passes the latent encoding z through two linear layers with ReLU activation functions and a transposed VQ-VAE backbone, outputting the OGM prediction $\hat{\mathcal{M}}_h$.

To avoid latent space collapse, we clamped the KL divergence term in the loss in Eq. (2) at 0.2. Additionally, we anneal the β hyperparameter in the loss according to a sigmoid schedule as recommended by Bowman et al. [44]. In our hyperparameter search, we found a maximum β of 1 with a crossover point at 10,000 iterations to work well. The β hyperparameter increases from a value of 0 to 1 over 1,000 iterations. We set the α hyperparameter to 1.5. We trained the network with a batch size of 256 for 30 epochs using the Adam optimizer [45] with a starting learning rate of 0.001.

A.4 Multi-Sensor Fusion Experimental Details

To perform sensor fusion, a correspondence between the grid cells of a predicted driver sensor OGM $\hat{\mathcal{M}}_h$ and the ego vehicle’s OGM \mathcal{M}_{ego}^{obs} needs to be found. For each occluded grid cell ($\mathcal{M}_{ego}^{obs} = 0.5$), the corresponding cell in $\hat{\mathcal{M}}_h$ is identified to transfer the occupancy information. We first transform both grids to a global frame. We use a k-d tree [46] of the grid cells in $\hat{\mathcal{M}}_h$ in the global frame to find the nearest neighbor match for each occluded grid cell in \mathcal{M}_{ego}^{obs} . Cells that do not have a match have a default distance of infinity. We further set a distance tolerance of 1 m to ensure only reasonable nearest neighbor cells are found. If no nearest neighbor cell is identified from $\hat{\mathcal{M}}_h$, the occluded grid cell probability remains unchanged in \mathcal{M}_{ego}^{obs} as 0.5. This process is repeated for each observed driver h , producing a collection of estimated OGMs $\hat{\mathcal{M}}_h$ in the ego vehicle’s frame of reference. The collection is then fused into a single updated grid $\hat{\mathcal{M}}_{ego}$ according to the evidential sensor fusion procedure described in Section 4.

To compute the multimodality metrics for the full occlusion inference pipeline in Table 2, we had to determine the three most likely modes for each time step according to the likelihood of $\hat{\mathcal{M}}_{ego}$: $p(\hat{\mathcal{M}}_{ego}) = \prod_h p_\theta(z | s_h^{1:T})$ for all visible drivers h . To avoid computing intractably many products for all the modes for each sensor driver, we use breadth-first search to find the three most likely modes for the multimodality metrics.

A.5 Image Similarity Metric

The IS metric ψ is computed as follows [39]:

$$\begin{aligned} \psi(\mathcal{M}_1, \mathcal{M}_2) &= \sum_{a \in \{0,1\}} d(\mathcal{M}_1, \mathcal{M}_2, a) + d(\mathcal{M}_2, \mathcal{M}_1, a) \\ d(\mathcal{M}_1, \mathcal{M}_2, a) &= \frac{1}{\#_a(\mathcal{M}_1)} \sum_{\mathcal{M}_1[i,j]=a} \min \{ \|g(i,j) - g(k,l)\|_1 : \mathcal{M}_2[k,l] = a \} \end{aligned} \quad (6)$$

where \mathcal{M}_1 and \mathcal{M}_2 are OGMs, $\mathcal{M}_1[i,j]$ is the occupancy class at grid cell (i,j) in OGM \mathcal{M}_1 , $g(\cdot)$ is the 2D spatial coordinate for each cell in the OGM. Here, $\|\cdot\|_1$ denotes the Manhattan distance between the spatial coordinates, and $\#_a(\mathcal{M}_1)$ is the number of cells in \mathcal{M}_1 with occupancy class a .

We consider only the grid cells that have an occupancy probability thresholded to occupied (i.e., for probability ≥ 0.6 , $\mathcal{M}[i,j] = 1$) or free (i.e., for probability ≤ 0.4 , $\mathcal{M}[i,j] = 0$). Unknown cells (i.e., for $0.4 < \text{probability} < 0.6$, $\mathcal{M}[i,j] = 0.5$) are ignored in the computation.

A.6 Further Details on the K-means PaS and GMM PaS Baselines

The first step in both the k-means PaS and GMM PaS driver sensor model baselines is to cluster the trajectories $s_h^{1:T}$ in the training data. We have $K = 100$ clusters for each model. Then given a cluster z_k , where $k = \{1, \dots, K\}$, the occupancy probability of each cell in $\hat{\mathcal{M}}_h$ for an observed driver h is computed. The grid cells are assumed to be independent of each other. For each grid cell c and cluster z_k , we can compute the occupancy probability in the driver sensor OGM using Bayes’ Rule, i.e.,

$$\hat{\mathcal{M}}_{h,c} = p(a_c = 1 | z_k) = \frac{p(z_k | a_c = 1)p(a_c = 1)}{p(z_k)} \quad (7)$$

where $a_c \in \{0, 1\}$ is the occupancy class. We assume $p(a_c)$ is uniform over the occupied and free classes (i.e., $p(a_c) = 0.5$). From the law of total probability, we have

$$\hat{\mathcal{M}}_{h,c} = p(a_c = 1 | z_k) = \frac{p(z_k | a_c = 1)p(a_c = 1)}{\sum_{a_c \in \{0,1\}} p(z_k | a_c)p(a_c)} = \frac{p(z_k | a_c = 1)}{p(z_k | a_c = 1) + p(z_k | a_c = 0)}. \quad (8)$$

The term $p(z_k | a_c)$ is computed by dividing the number of occurrences of z_k and a_c together in the training set by the number of occurrences of a_c according to the definition of conditional probability.

B Results

B.1 Decoded Latent Classes

The decoded latent spaces for each of the considered driver sensor models: k-means PaS, GMM PaS, and CVAE (ours), are shown in Fig. 6. The latent spaces of k-means PaS and GMM PaS are quite similar as can be expected due to the structural similarities between both models. However, the CVAE is distinct from the baselines in that the decoded occupancy values appear higher (likely due to the weighted reconstruction loss that favors occupied classes) and more localized. There is a higher number of decoded OGMs for the CVAE that only have localized occupancy regions as opposed to mostly occupied or unknown space as in the k-means PaS and GMM PaS models. Generally, the baselines tend to predict more unknown space in the OGMs than the CVAE.

B.2 Additional Multi-Agent Occlusion Inference Baselines

We consider two additional baselines for the multi-agent occlusion inference pipeline: a naive averaging strategy in place of the proposed evidential sensor fusion approach and the vanilla OGM \mathcal{M}_{ego}^{obs} which has 0.5 probability in occluded cells and does not have any occlusion inference. The results of these two baselines and our proposed method with evidential sensor fusion for reference are shown in Table 3. This table is an extension of Table 2.

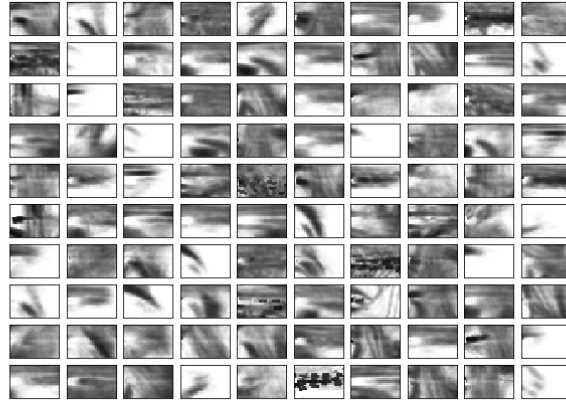
The vanilla OGM baseline serves as a sanity check, but does not provide meaningful metric results as all the occupancy values are set to 0.5. This yields an accuracy of 0 and an MSE of 0.25. In the IS metric, the constant occupancy value of 0.5 manifests itself in having the maximum Manhattan distance for the free and occupied cells in the ground truth OGM. However, the IS metric includes distances from both the predicted OGM and the ground truth OGM, which serves as an advantage for the vanilla OGM. The distances from the predicted OGM to the ground truth grid cells are 0 since 0.5 values are ignored in the computation (see Appendix A.5), thus lowering the IS metric value. The metrics are computed over the occluded regions in \mathcal{M}_{ego}^{obs} and where the k-means PaS baseline does not predict unknown space. The vanilla OGM outperforms our proposed methods for the MSE and IS metrics in the occupied class according to Table 3. The MSE metric is biased to 0.5 values, preferring them over a more confident, but imprecise occupancy prediction. The IS metric is artificially lower for the vanilla OGM in the occupied class because the ground truth has relatively few occupied cells, and there are no predicted occupied cells in the vanilla OGM, unlike the driver sensor models.

Table 3: Our method outperforms baseline approaches across most considered metrics for the full occlusion inference pipeline. Metrics are computed on the most likely discrete latent class. Best of 3 most likely latent classes are denoted as “Top 3” metrics. Note that IS values are divided by 100. The maximum standard error per grid cell in MSE and accuracy metrics is 0.0008, and per occupancy grid in the IS metric is 0.0046.

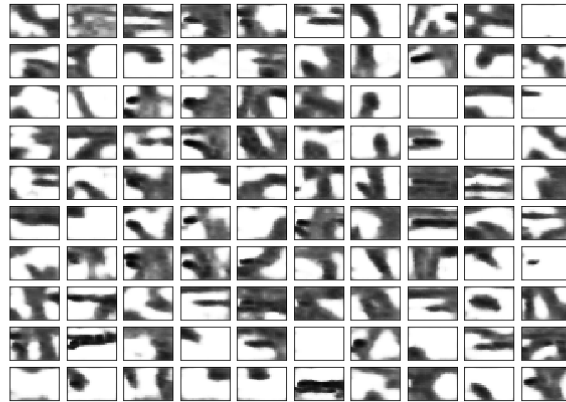
Method	Occupied	Free	Overall	Occupied	Free	Overall
	Acc. ↑			Top 3 Acc. ↑		
Vanilla OGM	0	0	0	N/A	N/A	N/A
Ours (Average)	0.693	0.721	0.721	0.762	0.770	0.768
Ours (Evidential)	0.660	0.722	0.722	0.746	0.778	0.774
	MSE ↓			Top 3 MSE ↓		
Vanilla OGM	0.250	0.250	0.250	N/A	N/A	N/A
Ours (Average)	0.269	0.166	0.167	0.214	0.135	0.138
Ours (Evidential)	0.303	0.171	0.173	0.233	0.136	0.140
	IS ↓			Top 3 IS ↓		
Vanilla OGM	0.974	2.600	3.573	N/A	N/A	N/A
Ours (Average)	1.345	0.019	1.364	1.229	0.013	1.243
Ours (Evidential)	1.336	0.017	1.353	1.220	0.011	1.232



(a) K-means PaS



(b) GMM PaS



(c) Ours

Figure 6: Decoded latent classes from the considered driver sensor models. Our model produces higher occupancy values in more localized regions than the baselines, which tend to predict mostly lower valued occupied or unknown space.

Interestingly, the naive averaging strategy performed comparably to evidential sensor fusion in Table 3. A potential reason for this could be the spatial bias introduced by including the occlusion inference only in regions of occlusion from the ego vehicle. These regions often do not contain the interaction for the driver sensor (e.g., to the side of the driver). Averaging outperformed evidential sensor fusion on the MSE metric. We hypothesize that this might be due to the averaged predicted values being closer to 0.5 than those from the evidential sensor fusion. This leads to improvement in the MSE metric as it is biased towards 0.5 probabilities. In line with this hypothesis, we found in our experiments that the averaging approach resulted in a slightly higher number of predicted cells being thresholded to 0.5 as compared to the evidential sensor fusion technique. In the IS metric, our method with evidential sensor fusion outperformed averaging, showing better captured structure of the inferred environment.

B.3 Further Analysis for the Multi-Agent Occlusion Inference Pipeline

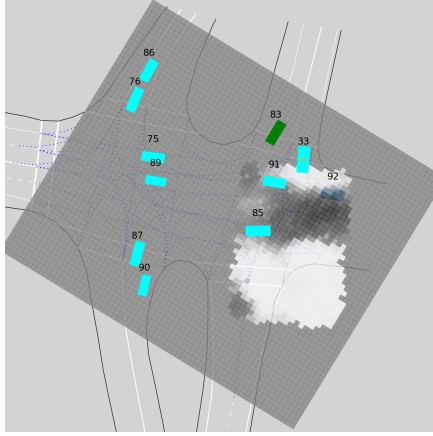
B.3.1 Individual Predictions for Observed Drivers

In Fig. 7, we illustrate the individual predictions for some of the observed drivers in the scene depicted in Fig. 4. The predicted OGMs $\hat{\mathcal{M}}_h$ are shown within the ego vehicle’s OGM, which, for easier visualization, is assumed to be entirely occluded. As expected, the CVAE driver sensor model predicts the stopped vehicles (Figs. 7a and 7d) to have occupied space ahead and to the left of them (where oncoming traffic is approaching from). Driver 85, who is moving at a constant speed, further adds to the occupied space prediction of driver 33 as traffic often exists in that lane in the dataset. As driver 33 starts moving (Fig. 7c), the space ahead and to the left of them is predicted as free, signaling to the ego vehicle that it may be safe to turn right. The space to the right of driver 33 may be occupied with cars that have passed by, but these cars do not affect driver 33’s left turn maneuver. These occlusion inference results align with our intuition for the task.

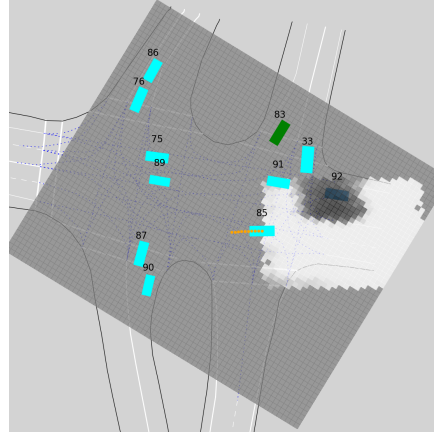
B.3.2 Multimodal Predictions for Multi-Agent Occlusion Inference

We further investigate the benefits of modeling distributional multimodality for the multi-agent occlusion inference pipeline. In Fig. 8, we consider two observed constant speed drivers 75 and 89 and their top two most likely predicted modes for the scene in Fig. 4. Again, the predicted OGMs $\hat{\mathcal{M}}_h$ are shown within the ego vehicle’s OGM, which, for easier visualization, is assumed to be entirely occluded. We would expect that the distribution over the latent space would capture the possibility that there is free or occupied space ahead of these drivers, corresponding to driving in an empty lane or in traffic. The results show that the top two decoded modes are the same for both drivers. One mode predicts free space ahead with occupied space to the sides (i.e., driving in an open lane), and the other mode predicts occupied space ahead (i.e., driving behind traffic in the same lane). The CVAE outputs almost equal likelihoods for these two modes for driver 75. For driver 89, the occupied space ahead mode is more likely. This could be due to the dataset statistics in this location of the intersection favoring traffic ahead of the driver.

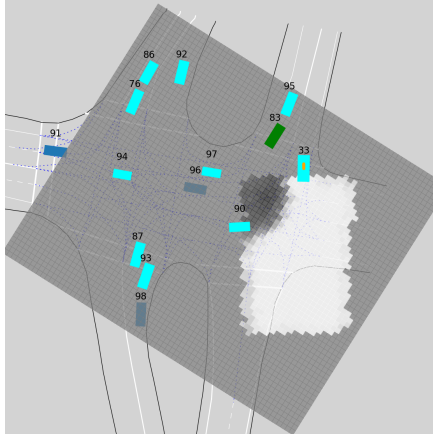
In Fig. 9, we analyze how the predicted multimodality for these constant speed drivers manifests itself in the full occlusion inference pipeline. We consider all the possible combinations of the OGMs corresponding to the top two most likely modes for drivers 75 and 89. We use the most likely modes for the predicted OGMs for the remaining observed drivers. In Fig. 9b, both drivers have OGMs that predict traffic ahead, resulting in high occupancy levels predicted ahead of these vehicles in the fused ego vehicle OGM. In Fig. 9c, both drivers have OGMs that predict free space ahead, thus their combination in the fused ego vehicle OGM yields the lowest occupancy probability ahead out of the available possibilities. In practice, to ensure tractability, a set number of most likely inferred ego vehicle OGMs could be considered by a planning algorithm. We hypothesize that incorporating the multimodal options into the planner would result in more proactive and informed behavior by the ego vehicle. High distributional multimodality may also be an indication that there is insufficient information provided by the observed driver behavior to confidently infer the occupancy of the space ahead.



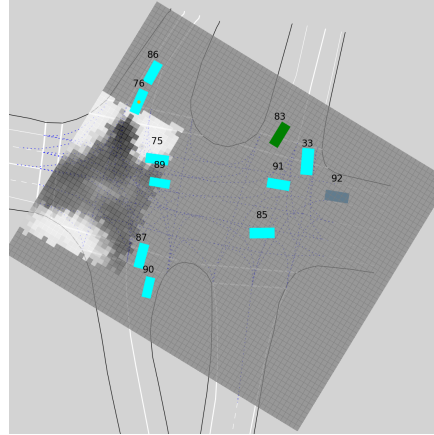
(a) Vehicle 33: stopped.



(b) Vehicle 85: constant speed.



(c) Vehicle 33: accelerating.



(d) Vehicle 76: stopped.

Figure 7: Individual predictions for some of the observed drivers for the scene in Fig. 4 using our proposed CVAE driver sensor model. The observed drivers are shown in cyan and their trajectories for the past 1 s ($s_h^{1:T}$) in orange. We focus on the observed drivers 33, 76 and 85. The predicted OGMs $\hat{\mathcal{M}}_{33}$, $\hat{\mathcal{M}}_{76}$, and $\hat{\mathcal{M}}_{85}$ are shown for their most likely latent mode within the ego vehicle's OGM, which is assumed to be fully occluded for easier visualization. The OGMs depict free (white), occluded (gray), and occupied (black) space. The OGMs in Figs. 7a, 7b and 7d are from the same time step as Fig. 4a. The OGM in Fig. 7c is from the same time step as Fig. 4b. The CVAE infers occupied space ahead for the stopped vehicles (Figs. 7a and 7d). For the moving vehicle in Fig. 7c, the CVAE yields mostly free space. The constant speed vehicle 85 is predicted to have occupied space where traffic commonly exists. These qualitative results match our intuition for the occlusion inference task.

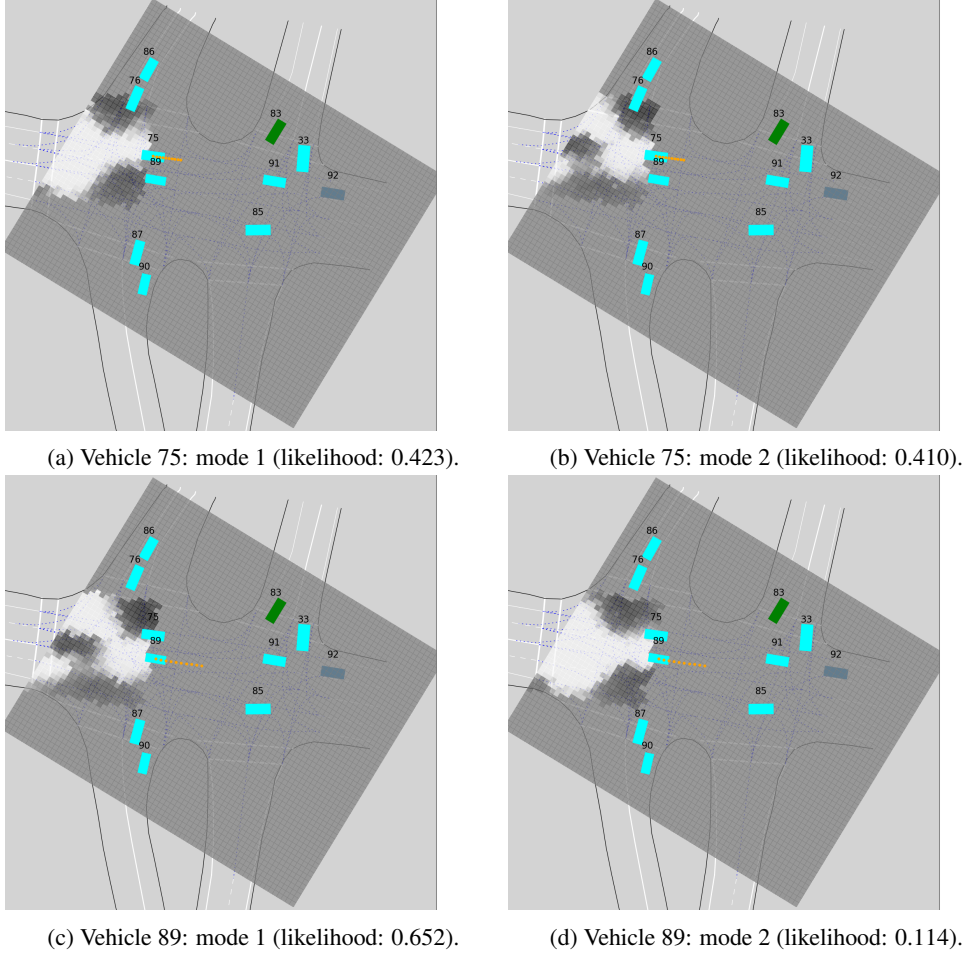
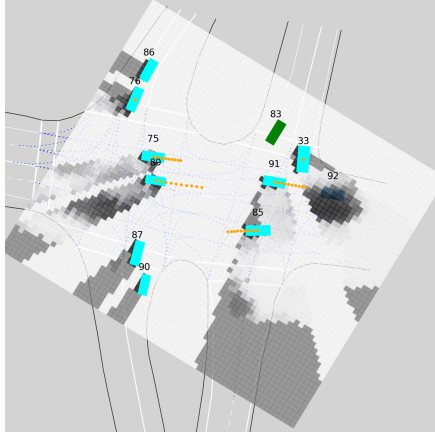


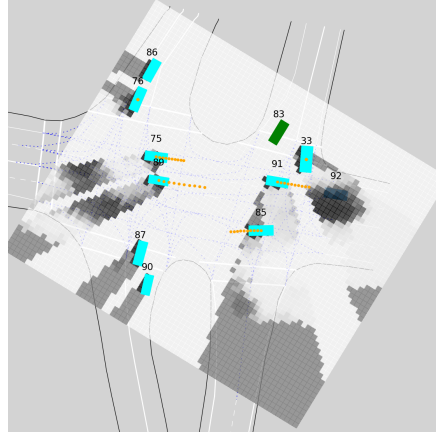
Figure 8: Multimodal results for the full pipeline using our proposed CVAE driver sensor model for the scene in Fig. 4. The observed drivers are shown in cyan and their trajectories for the past 1 s ($s_h^{1:T}$) in orange. We focus on the observed drivers 75 and 89, who are moving at a constant speed. The predicted OGMs $\hat{\mathcal{M}}_{75}$ and $\hat{\mathcal{M}}_{89}$ are shown for their top two most likely latent modes within the ego vehicle’s OGM, which is assumed to be fully occluded for easier visualization. The OGMs depict free (white), occluded (gray), and occupied (black) space. As expected, the top two most likely modes for both drivers depict either free or occupied space ahead. The observed constant speed trajectories are insufficient to discern the environment ahead of the drivers with confidence.

B.4 Additional Multi-Agent Occlusion Inference Pipeline Example

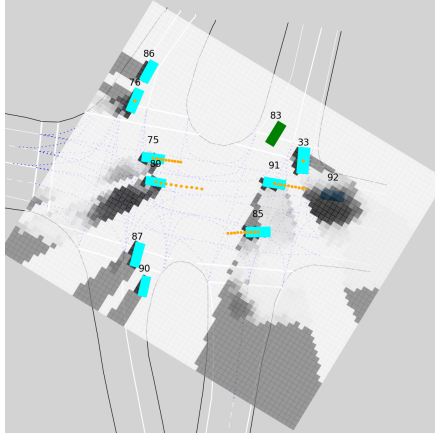
Fig. 10 illustrates an additional scenario with two different observed behaviors by a driver sensor. The ego vehicle (green) is waiting to turn left behind another vehicle at the unsignalized intersection. There are several observed drivers around the ego vehicle. Driver 106 ahead of the ego vehicle is waiting to turn left and is blocking the view of oncoming traffic. In Fig. 10a, observed drivers 106, 113, 102, and 116 are all stopped due to occluded driver 112 passing by. The CVAE driver sensor model predicts occupied space ahead for each of these observed drivers (see Fig. 11). The fused measurements in the region of occlusion for the ego are thus inferred to be highly occupied. Our multi-agent occlusion inference algorithm is thus able to correctly identify occupied space in the vicinity of occluded driver 112. In Fig. 10b, driver 106 starts moving to make the left turn as there is a gap in traffic. Our method successfully infers free space ahead of this driver, indicating to the ego vehicle that it may be safe to proceed with its own maneuver (e.g., a U-turn or a left turn). In both cases, our approach is able to provide additional insight about the scene to the ego vehicle as compared to the vanilla OGM \mathcal{M}_{ego}^{obs} with no occlusion inference.



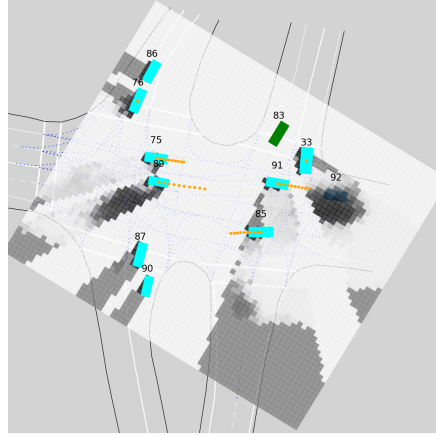
(a) Vehicle 75: mode 1, Vehicle 89: mode 1.



(b) Vehicle 75: mode 2, Vehicle 89: mode 1.

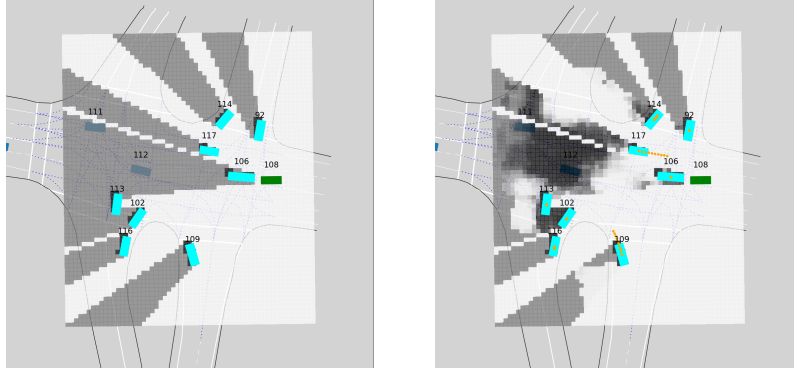


(c) Vehicle 75: mode 1, Vehicle 89: mode 2.

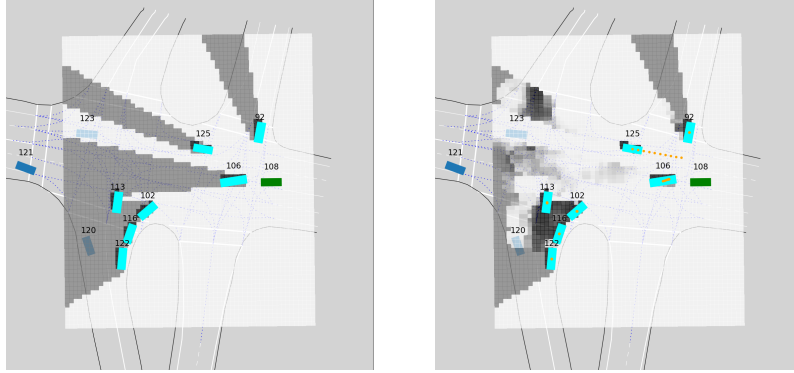


(d) Vehicle 75: mode 2, Vehicle 89: mode 2.

Figure 9: Multimodal results for the full pipeline using our proposed CVAE driver sensor model for the scenario in Fig. 4. The scenario depicts the ego vehicle (green) waiting to make a left turn. The observed drivers are shown in cyan and their trajectories for the past 1 s ($s_h^{1:T}$) in orange. The occluded vehicles are shown in blue. We consider the top two most likely modes for drivers 75 and 89. The fused OGM $\hat{\mathcal{M}}_{ego}$ (right) depicts free (white), occluded (gray), and occupied (black) space around the ego. The inferred occupancy predictions by the algorithm accurately capture the multimodal possibilities for the occluded space ahead of the observed drivers.

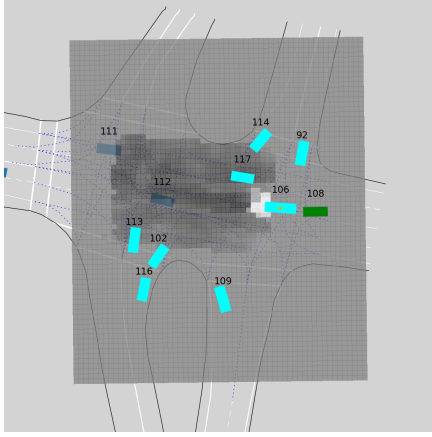


(a) Stopped vehicle.

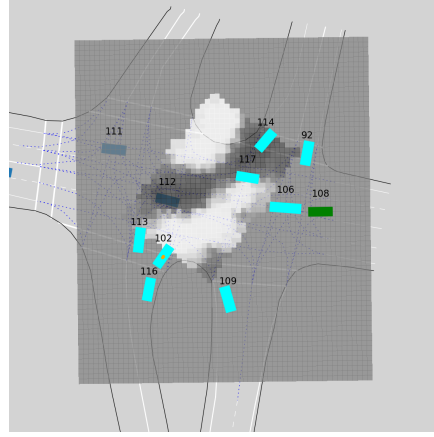


(b) Acceleration maneuver.

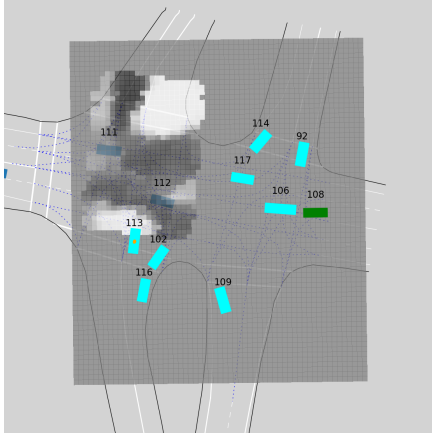
Figure 10: Additional qualitative results for the full pipeline using our proposed CVAE driver sensor model. The scenario depicts the ego vehicle (green) waiting to make a left turn. The observed drivers are shown in cyan and their trajectories for the past 1 s ($s_h^{1:T}$) in orange. The occluded vehicles are shown in blue. The vanilla OGM \mathcal{M}_{ego}^{obs} (left) and the fused OGM $\hat{\mathcal{M}}_{ego}$ (right) depict free (white), occluded (gray), and occupied (black) space around the ego. The inferred occupancy predictions by the algorithm match the ground truth and our intuition based on the observed behaviors.



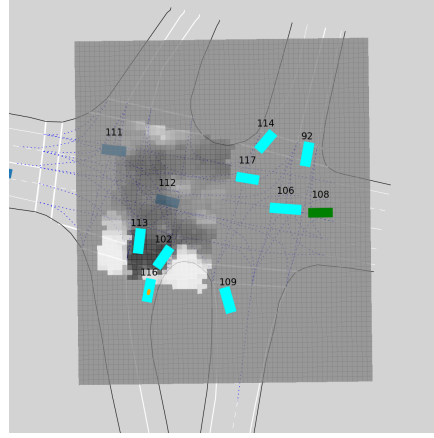
(a) Vehicle 106 (stopped).



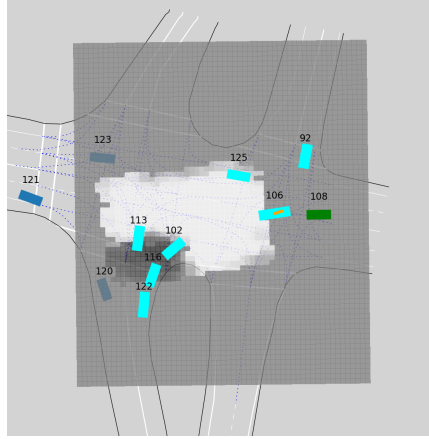
(b) Vehicle 102 (stopped).



(c) Vehicle 113 (stopped).



(d) Vehicle 116 (stopped).



(e) Vehicle 106 (moving).

Figure 11: Individual predictions for some of the observed drivers in the scene in Fig. 10 using our proposed CVAE driver sensor model. The observed drivers are shown in cyan and their trajectories for the past 1 s ($s_h^{1:T}$) in orange. We focus on the observed drivers 106, 102, 113, and 116. The predicted OGMs $\hat{\mathcal{M}}_{106}$, $\hat{\mathcal{M}}_{102}$, $\hat{\mathcal{M}}_{113}$, and $\hat{\mathcal{M}}_{116}$ are shown within the ego vehicle's OGM, which, for easier visibility, is assumed to be entirely occluded. The OGMs depict free (white), occluded (gray), and occupied (black) space. The CVAE driver sensor model successfully infers occupied space in the oncoming traffic lanes for the ego vehicle based on observed stopped vehicles, and free space in that region based on an observed accelerating vehicle.